

Direct Observation of Hydrogen Spillover in Ni-Loaded Pr-Doped Ceria

Vaneet Sharma^a, Peter A. Crozier^a, Renu Sharma^{a,b}, and James B. Adams^a

^a*School for Engineering of Matter, Transport and Energy, Arizona State University, Tempe, Arizona 85287-6106*

^b*Center for Nanoscale Science and Technology, National Institute of Standards and Technology, Gaithersburg, MD 20899-6203*

Abstract

In situ studies on reduction processes in Pr-doped ceria and Ni-loaded doped ceria nanoparticles have been investigated using environmental transmission electron microscopy. The presence of pit-like defects on the oxide nanoparticles resulted in amorphization during reduction. Hydrogen-spillover in Ni-loaded Pr-doped ceria (PDC) was directly observed. Localized reduction of ceria in a H₂ atmosphere was observed and attributed to gas-Ni-ceria interactions at the three-phase boundary. The spatial extent of the localized reduction zones was experimentally determined. The spillover mechanism is discussed in terms of surface diffusion properties of atomic hydrogen and oxygen species.

Keywords: *In-situ*, Pr-doped ceria, reduction zone, hydrogen-spillover, TEM.

Corresponding Author: P.A. Crozier

Email: crozier@asu.edu

Tel: 1 480 965 2934

Fax: 480 727 9321

1. Introduction

Solid oxide fuel cells (SOFC) are a promising technology for efficient conversion of chemical fuels into electricity. In a SOFC, a cathode converts gaseous oxygen into oxygen ions, these ions diffuse through an electrolyte to an anode where they oxidize a fuel resulting in the release of electrons. The electrons are collected and used to drive an external circuit before returning to the cathode. SOFCs are attractive because they can utilize a variety of different fuels (hydrogen, hydrocarbon, carbon monoxide etc.) and the electrocatalysts are more resistant to feedstock impurities [1]. In principle, fuel flexibility combined with poison resistance should allow SOFCs to operate without the need for extensive and expensive fuel processing. At present most SOFCs are based on yttria stabilized zirconia (YSZ) and typically operate at temperatures in excess of 1000 °C. The anode, cathode and electrolyte are composed of ceramic materials with metal contacts and high operating temperatures can lead to challenging materials problems that negatively affect cell performance. Components undergo a variety of solid-state and gas-solid reactions that may result in a breakdown in the electronic and ionic conduction paths and mechanical failure due to delamination [1]. Current Ni/YSZ based anodes are also vulnerable to deactivation due to coking when hydrocarbon fuels are employed.

Many of the materials problems associated with SOFC operation may be greatly mitigated by reducing the operation temperature of the cell. To accomplish this goal, it is necessary to develop electrode and electrolyte materials that have respectively high catalytic activities and ion conductivities at low temperatures. Cerium-based oxides are currently being investigated as possible anode materials for SOFC operating temperatures in the range 500-700°C. We are especially interested in the cermet

(metal intermixed with ceramic material) anodes based on Ni metal combined with Gd and Pr doped ceria [2]. In order to optimize the properties of a cermet material, it is important to develop a fundamental understanding of the dynamic processes taking place at the anode during fuel cell operation.

We have investigated Pr doped ceria (PDC) as a promising anode material for intermediate-temperature (500 °C to 700 °C) solid-oxide-fuel-cells (IT-SOFCs) [3-6]. The oxygen ion conductivity of this material is 2 to 3 order of magnitude higher than pure ceria at 700 °C [7], and has been attributed to the presence of high concentrations of oxygen vacancies created during a low temperature (≈ 200 °C) reduction of Pr^{4+} to Pr^{3+} [8, 9]. We are interested in using *in situ* environmental transmission electron microscopy (ETEM) to investigate the nanoscale interfacial interactions that take place at the Ni-PDC interface at elevated temperature in a reducing atmosphere. This closely corresponds to the typical operating conditions of a real SOFC anode. Many different processes are likely to take place on the anode during fuel cell operation including PDC reduction, grain boundary segregation, three phase boundary reactions and solid state reactions between the Ni and ceria. Here we focus on employing ETEM to investigate a spillover phenomenon associated with the three-phase boundary at the gas-Ni-ceria interface leading to the formation of localized reduction zones. The spillover mechanism plays an important role in many gas phase catalytic reactions and there have been a considerable number of experimental and theoretical studies of this process [10-14]. However, to our knowledge there have been no direct electron microscopy observations of this phenomenon in terms of local chemical changes in Ni/rare-earth doped ceria systems.

2. Experimental

Pure ceria and 10 mole fraction (%) Pr doped ceria (PDC) nanopowders were synthesized via a spray drying method as described in detail elsewhere [15]. As-synthesized powders were heat treated in a box furnace at 700 °C for 2 h to obtain crystalline nanoparticles. 0.1 mass fraction Ni was loaded onto the PDC powder using conventional wet impregnation techniques. PDC powder was first impregnated with $\text{Ni}(\text{NO}_3)_3 \cdot 6\text{H}_2\text{O}$ solution in ethanol using an incipient wetness approach. The impregnated powder was then dried at 200 °C in air followed by a direct reduction at 400 °C for 4 h in a flowing mixture of 0.05 volume fraction hydrogen in helium in a single-zone tube furnace to convert $\text{Ni}(\text{NO}_3)_3$ to Ni metal. TEM samples were prepared by crushing the nanopowders between two glass slides to break the particle agglomerates and dry loading the powder onto 3 mm Pt grids punched out from 200 mesh Pt gauge. These grids were then loaded in a TEM heating holder and introduced into the column of an FEI Tecnai F20* environmental transmission electron microscope (ETEM). Samples were progressively heated to 700 °C in flowing hydrogen pressure of 130 Pa for *in situ* reduction. High resolution images, electron diffraction patterns and electron energy-loss spectra (EELS) were recorded at specific temperatures of interest to investigate the morphological and chemical changes in the nanoparticles. *Ex-situ* reduction was carried out in a single zone tube furnace at 900 °C for 6 h in a flowing mixture of 0.05 volume fraction hydrogen in helium.

3. Results and Discussion

3.1 *In-situ* reduction of pure ceria and PDC

The morphological changes occurring during the *in-situ* reduction of pure ceria and PDC were investigated by analyzing high-resolution images acquired before and after *in-situ* reduction in

hydrogen. The degree of crystallinity in the particles was determined by monitoring the visibility of lattice fringes and the characteristic speckle pattern associated with an amorphous material, in the high resolution images. Selected area electron diffraction patterns acquired from nanoparticle clusters were additionally used to estimate the crystallinity of the particles by observing the nature of diffraction spots. High-resolution images of a typical pure ceria nanoparticle acquired at 200 °C in vacuum and after *in-situ* reduction in hydrogen at 700 °C are shown in Fig. 1. The crystalline nature of the particle shown in Fig. 1(a) is obvious from the presence of the characteristic 0.31 nm lattice fringes corresponding to CeO₂ {111} planar spacing. Sharp diffraction spots in the selected area diffraction pattern (inset of Fig. 1(a)), which arise due to Bragg reflections from a well-ordered fluorite crystal structure, further confirm the crystalline nature of PDC nanoparticle. The same nanoparticle after *in-situ* exposure to 130 Pa hydrogen at 700°C is shown in Fig. 1(b). Loss of crystallinity in this particle is apparent from the reduced visibility of lattice fringes and the pronounced speckle contrast in the high-resolution image. Moreover, the selected area diffraction pattern acquired from the same cluster after reduction shows the presence of diffuse rings along with some Bragg spots as shown in the inset of Fig. 1(b). The presence of diffuse rings, which arise due to diffraction from a highly defective or amorphous solid, confirmed that the material had undergone partial amorphization during reduction.

Cerium reduction in the particles was confirmed with electron energy-loss spectra acquired from the same cluster of nanoparticles. The reversal of the relative heights of the Ce M_{4,5} white lines is an indication of changes in the oxidation state with a higher M₅/M₄ ratio indicating the presence of a +3 oxidation state [16]. Insets in Fig. 1(a) and 1(b) respectively show the energy-loss spectra acquired

from the nanoparticle cluster before and after *in-situ* reduction. The oxidation state of Ce at 200 °C was found to be 3.8 ± 0.1 while after heating to 700 °C in hydrogen it reduced to 3.1 ± 0.1 .

Similar loss of crystallinity was also observed in the PDC sample after *in-situ* reduction at 650 °C as shown in Fig 2(a) and 2(b). The amorphization of the material was correlated with reduction in hydrogen and not electron beam damage. Sharma et al [16] have measured the effects of electron dose on the chemical changes (oxidation state) of Ce in pure ceria. They found that significant changes occurred in the Ce white lines with an electron dose of 2×10^7 electrons /nm² at room temperature. For the current experiments, we kept the electron dose below $\approx 10^6$ electrons nm⁻², and did not observe any significant changes in the image and in the Ce M₅/M₄ ratio in the absence of hydrogen

3.2 *Ex-situ* reduction of PDC

Ex-situ reduction was performed on a crystalline and fully oxidized PDC sample to validate the *in-situ* observations. Figure 3(a) shows a high-resolution image of a typical nanoparticle at room temperature before reduction. A high degree of crystallinity is evident from the sharp and continuous lattice fringes in the particle along with well-defined surface facets. The inset of Fig. 3(a) shows an energy-loss spectrum acquired from this particle indicating that ceria was present in an oxidized form. The sample was then reduced *ex situ* in a tube furnace at 900 °C for 6 h. After reduction and subsequent examination in the TEM at 200 °C, a highly pronounced speckle contrast pattern indicating amorphization of the material was clearly seen in the high-resolution image, Fig. 3(b). The energy-loss spectrum acquired from this sample (inset of Fig. 3(b)) showed that re-oxidation of ceria after cooling and subsequent exposure to air (during transfer to TEM) did not result in the re-crystallization.

Other researchers have employed thermogravimetry and *in-situ* x-ray diffraction techniques to investigate changes in ceria during reduction although they do not report any data on amorphization [17-19]. In our previous work on ceria samples prepared using a precipitation technique, such amorphization was not observed during reduction. *In situ* observations showed that ceria reduction often resulted in the oxygen vacancy ordering, giving rise to a superstructure [20,21]. However, not only were these samples synthesized differently, they were heated in air to 1000°C prior to *in situ* reduction. As a result, the grain size in the starting material was substantially larger and the crystallites were mostly defect free compared to the material investigated here.

The current starting materials often have a large number of pit-like defects present as a result of the spray drying and relatively low calcination temperature (see Fig. 1(a), 2(a) and 3(a)). The sides of the pit defects are composed of (111) nanofacets and in some cases dislocations are also observed in the nanocrystals. These pit-like defects may inhibit the formation of extended oxygen vacancy ordering of the reduced structure. Evidence for the role of pit-like defects on the amorphization was found by investigating the particles which were free from such defects. A typical example of such a particle is shown in Fig 4(a). Upon *in-situ* heating in H₂, this particle did not undergo amorphization as shown in Fig. 4(b), although it did undergo reduction as indicated by the energy-loss spectrum shown in the inset of Fig. 4(b).

For the highly ordered materials, the oxygen vacancy ordered structure is associated with a phase transformation where the fluorite structure (S.G. Fm-3m) transforms to a body center cubic structure

(Ia-3) associated with small atomic displacements [18,19]. As reported earlier, the vacancy ordering in the fluorite structure is constrained by the structural principles as outlined by Kang et al. [22]. Vacancy pairs line up along the $\langle 111 \rangle$ directions which preserves the cubic symmetry and leads to extended domains of vacancy ordering. In the spray dried materials, when oxygen vacancies are introduced during reduction, the pit defects disrupt vacancy ordering and appear to destabilize the cubic structure resulting in amorphization. When the sample is cooled, the Ce^{+3} re-oxidizes to Ce^{+4} but kinetic limitations associated with the lower oxidation temperature prevent the fluorite structure from reforming.

3.3 *In-situ* reduction of Ni loaded PDC

Ni loaded PDC powder sample was first pre-reduced *ex-situ* at 900 °C for 6 h. For *in-situ* reduction, the sample was first heated to 420 °C in flowing hydrogen gas at 130 Pa and held for 2 h to reduce NiO (formed during exposure of Ni particles to air after pre-reduction step) to Ni metal particles. Fig. 5(a) shows a high-resolution image of a typical Ni particle on PDC support at 420 °C. Speckle contrast seen near the Ni particle indicates preferential amorphization in the vicinity of the Ni particle which is an indication preferential reduction of the PDC in the vicinity of the Ni particle. Energy-loss spectra were acquired from two regions, each from approximately 5 nm in diameter, within the same PDC nanoparticles (Fig. 5). A background subtracted energy-loss spectrum from Area 1 is shown in Fig. 5(b). The presence of Ni-L₃ and Ni-L₂ edges in the spectrum, at 855 eV and 872 eV, respectively indicate that the specified region was in close proximity to the Ni particle. The higher intensity in Ce-M₅ as compared to Ce-M₄ indicates that Ce is present in a reduced state in this region. The measured oxidation state of Ce in this region was around 3.2 ± 0.1 . Area 2 as marked in Fig. 5(a) was selected at

a distance of approximately 15 nm away from the interface. Energy-loss spectrum from this region is shown in Fig. 5(c) and indicates the presence of Ce in a partially reduced state with the measured oxidation state of 3.5 ± 0.1 .

Similar measurements were performed on several different Ni-PDC interfaces and all showed preferential reduction of the PDC particle in the vicinity of Ni particle (see Table 1). PDC does not reduce until 650 °C and the low temperature preferential reduction around Ni is a result of a spillover of highly reactive atomic hydrogen from Ni to PDC.

Determination of the spatial extent of the reduction zone was challenging because the average particle size was only 22 nm and there was substantial aggregation of the PDC particles leading to particle overlap in TEM image. However, an estimate of the spatial variation in the oxidation state was performed using a fairly large electron beam size (≈ 5 nm) to eliminate the possibility of any electron beam effects at these relatively low temperatures. First, the oxidation state of the ceria at the metal/PDC interface was determined. The electron beam was then moved as far from the interface as possible while still remaining on the PDC particle and avoiding particle overlap and additional Ni particles. A second measurement of the oxidation state was made at this second point. The oxidation state changes and corresponding distance from the interface are given in Table 1. It can be seen, that the small distances from the interface correspond to very small changes in the oxidation state. This is because it was not possible to move the probe further away from the Ni/ceramic interface either because the PDC particle was too small or because of overlap from surrounding PDC particles. Measurements 2 and 3 come from larger particles and suggest that the reduction zone around the Ni particles can extend up to 20 nm.

3.4 H Spillover from Metal onto Oxide

Catalytically active metals like Pt, Pd, Ru, Rh, Ni etc., have been found to significantly lower the temperature at which the reduction of the oxide support like ceria takes place [23-26]. Such an effect of metal loading on the oxide supports has been explained on the basis of hydrogen dissociation at the metal surface and its subsequent ‘spillover’ onto the oxide support [27, 28]. Spillover is defined as the transport of species (H, O, OH⁻ etc.) adsorbed on a first surface onto a second surface [29]. Ni dissociatively adsorbs hydrogen on its surface and the resulting atomic hydrogen can then be transported to the oxide support via hydrogen-spillover.

Different possible mechanisms for the reduction of the oxide support such as pure ceria have been suggested [30-33]. In the absence of re-oxidation, there are two processes that contribute to the formation of the reduction zone around the Ni particle. The first process involves dissociative adsorption of hydrogen on the Ni metal particles followed by spillover of atomic hydrogen onto the oxide support with reduction of the oxide at the interface. The second process is the migration of oxygen ions towards the interface and reaction with the spillover hydrogen at the interface. These two limiting cases are illustrated schematically in Fig. 6. In scheme 1 of Fig. 6(a) the spillover hydrogen atoms diffuse across the surface of PDC away from the Ni-PDC interface in all directions. Since the surface oxygen atoms are bonded by fewer nearest neighbors (lower co-ordination number than the bulk), they will initially readily combine with the highly reactive atomic hydrogen and form OH⁻ species. The surface OH⁻ species are known to ‘facilitate’ the surface diffusion of spillover hydrogen [34]. On combination with a second H atom, formation of H₂O takes place on the PDC surface. The

H₂O is readily desorbed from the surface and the surface oxygen is lost forming an oxygen vacancy at the surface. This surface vacancy readily diffuses into the bulk of PDC and the local stoichiometry is changed with a concomitant change in the Ce oxidation state. As more oxygen is lost from the surface, a reduction zone is formed around the Ni particle, which spreads in all directions.

Scheme 2 (Fig. 6(b)) mainly involves the diffusion of surface oxygen ions to the Ni/PDC interface. Initially the oxygen at the interface will be removed via reaction with spillover hydrogen creating a narrow zone of oxygen vacancies around the Ni particles. At high temperatures, the surface oxygen atoms can rapidly migrate via vacancy hopping across the surface to fill the vacancies at the Ni/PDC interface. With a continuous loss of oxygen ions at the interface via H₂O formation, the surface concentration of oxygen vacancies increases and these are backfilled by bulk oxygen ions. The average oxidation state of Ce is thus locally changed in the PDC around the Ni particle. A reduction zone is thus formed around the Ni particle, which then spreads spatially in all directions.

Which of these two schemes dominates is governed by the kinetics of surface diffusion on the oxide. (Since the surface diffusion of H on Ni is very fast, diffusion coefficient on the order of 10^{-11} m²/s, hydrogen spillover from Ni to PDC is not the rate-limiting step). Surface diffusion of the spillover species involves their transport along the surface of another solid and proceeds via a site-to-site hopping process. The rate-limiting step could then be the migration of atomic species, in this case H and O on the PDC surface. The diffusion coefficient for H migration on surface of a ceria based oxide at 400 °C is of the order of 2×10^{-17} m²/s whereas for surface oxygen, the diffusion coefficient is $6 \times$

10^{-16} m²/s [34, 35] which is an order of magnitude higher. This suggests that oxygen migration mechanism illustrated in Fig. 6(b) may dominate in this case.

The actual width of the reduction zone will not only depend on the reduction rate but also on the rate of re-oxidation of the sample. In the absence of atomically dissociated hydrogen, there is a strong thermodynamic driving force for Ce to remain in the +4 oxidation state at 400 °C. In our ETEM, the PDC will typically re-oxidize even in the H₂ atmosphere because of the residual oxygen partial pressure in the background gases of the microscope column. The Ni metal dispersion in this case is rather coarse (as it would be in a solid oxide fuel cell anode) and so some distance away from the metal particle the ceria reduction behavior would be independent of the presence of the metal. At 400 °C, the rate of re-oxidation exceeds the rate of reduction and the Ce remains in the +4 oxidation state. It is only close to the metal-ceramic interface where the concentration of atomic hydrogen is significant, that the rate of reduction exceeds the rate of re-oxidation leading to the formation of a reduction zone. Thus the reduction zone that we observed in the microscopy experiment provides information on the region around the Ni particle where the surface concentration of atomic hydrogen is high.

4. Conclusion

In-situ reduction of both pure ceria and PDC nanoparticles in hydrogen showed that the material amorphized upon reduction which was evidenced by high resolution imaging by TEM and additionally confirmed by selected area diffraction. *In-situ* results were validated by *ex-situ* experimentation and similar results were obtained. Amorphization of the nanoparticles was attributed to a possible effect of

'pit-like' defects present in the material as a result of the synthesis process. At high temperatures, the loss of oxygen atoms from these defective crystals leads to a substantial loss in long range order. It was also found that nanoparticles free from such pit-like defects showed a very stable crystal structure upon reduction under the same conditions. This suggested a strong role of defects in amorphization of the material upon reduction.

A preferential reduction of ceria in the vicinity of the Ni particle at temperatures much lower than the reduction temperature of pure PDC was observed. This interfacial effect was attributed to a hydrogen-spillover mechanism, which was directly evidenced by the presence of a reduction zone in PDC around the Ni particle. Energy-loss spectra acquired from two regions within the same nanoparticle showed that Ce was preferentially reduced in the vicinity of the Ni particle. The experimentally measured spatial extent of the reduction zone was found to be approximately 20 nm. Two possible mechanisms for the reduction zone formation were suggested, each involving the spillover of highly reactive atomic hydrogen from Ni to PDC. The formation and extent of the reduction zone was attributed to equilibrium between two cross-diffusing species (spillover hydrogen at the surface and surface oxygen ions).

5. Acknowledgements

We gratefully acknowledge the support from the US Department of Energy (DE-FG02-07ER46442) and John M. Cowley Center for High Resolution Microscopy at Arizona State University.

6. References

- [1] S.C. Singhal, and K. Kendall, *High Temperature Solid Oxide Fuel Cells: Fundamentals, Design and Applications*, 2003: Elsevier.
- [2] W.Z. Zhu, and S.C. Deevi, *Mat. Sci. & Eng.*, A362 (2003) 228-239.
- [3] A. Atkinson, S.B., R.J. Gorte, J.T.S. Irvine, A.J. Mcevoy, M. Mogensen, S.C. Singhal, J.Vohts, *Nature Materials*, 3 (2004) 17-27.
- [4] C. Sun and U. Stimming, *J. Power Sources*, 171(2007) 247-260.
- [5] M. Mogensen, N. M. Sammes, and G.A. Tompsett., *Solid State Ionics*, 129 (2000) 63-94.
- [6] S. Wang, T. Kato, S. Nagata, T. Honda, T. Kaneko, N. Iwashita, and M. Dokiya, *J. Electrochem. Soc.*, 149(7) (2002) A927-A933.
- [7] P. Shuk and M. Greenblatt, *Solid State Ionics*, **1999**, 116, 217.
- [8] H. Inaba, and K. Naito, *Solid State Ionics*, 50 (1983) 100.
- [9] C. López-Cartes, S. Bernal, J.J. Calvino, M.A. Cauqui, G. Blanco, J. A. Pérez-Omil, J.M. Pintado, S. Helveg, and P.L. Hansen, *Chem. Commun.*, (2003) 644.
- [10] G.M. Pajonk, *Appl. Catal. A: General*, 202(2000) 157-169.
- [11] S. J. Teichner, *Appl. Catal.*, 62(1990) 1-10.
- [12] T. Takeguchi, S.N. Furukawa, and M. Inoue, *J. Catal.*, 202(2001) 14-24.
- [13] D.H. Lenz, and W. C. Conner, *J. Catal.*, 112 (1988) 116-125.
- [14] L.F. Chen, J.A. Wang, M.A. Valenzuela, X. Bokhimi, D.R. Acosta, and O. Novaro, *J. Alloys and Comp.*, 417 (2006) 220-223.

- [15] V. Sharma, K. Eberhardt, R. Sharma, J.B. Adams, and P.A. Crozier, *Chem. Phys. Lett.*, 495 (2010) 280.
- [16] R. Sharma, P.A. Crozier, Z.C. Kang, L. Eyring, *Phil. Mag.*, 84 (2004) 2731-2747.
- [17] C. Lamonier, G. Wrobel and J.P. Bonnelle, *J. Mater. Chem.*, 4(12) (1994) 1927-1928.
- [18] J.L.G. Fierro, J. Soria, J. Sanz, and J.M. Rojo, *J. Solid State Chem.*, 66 (1987) 154-162.
- [19] V. Perrichon, A. Laachir, S. Abouarnadasse, O. Touret, and G. Blanchard, *Appl. Catal., A* 129 (1995) 69-82.
- [20] P.A. Crozier, R. Wang, and R. Sharma, *Ultramicroscopy*, 108 (2008) 1432-1440.
- [21] R. Wang, P.A. Crozier, R. Sharma, *J. Phys. Chem. C*, 113(2009) 5700-5704.
- [22] Kang reference
- [23] G. Vlaic, P.F., G. Martra, E. Fonda, J. Kaspar, L. Marchese, E. Tomat, S. Coluccia, and M. Graziani, *J. Catal.*, 190 (2000) 182-190.
- [24] P. Fornasiero, G.B., J. Kaspar, S. Meriani, R. Di Monte, M. Graziani, *Catal. Today*, 29 (1996) 47-52.
- [25] P. Fornasiero, J.K., V. Sergo, M. Graziani, *J. Catal.*, 182 (1999) 56-69.
- [26] H.W. Jen, G.W.G., W. Chun, R.W. McCabe, J.P. Cuif, S.E. Deutsch, and O. Touret, *Catal. Today*, 50 (1999) 309-328.
- [27] S. Salasc, V. Perrichon, M. Primet, M. Chevrier, and N. Mouaddib-Moral, *J. Catal.*, 189(2000) 401-409.
- [28] G.E.E. Gardes, G.M. Pajonk, and S.J. Teichner, *J. Catal.*, 33 (1974) 145-148.
- [29] W.C. Conner, and J.L. Falconer, *Chem. Rev.*, 95 (1995) 759-788.

- [30] M.K. Alam, F. Ahmed, R. Miura, A. Suzuki, H. Tsuboi, N. Hatakeyama, A. Endou, H. Takaba, M. Kubo, and A. Miyamoto, *Appl. Surf. Sci.*, 257 (2010) 1383-1389.
- [31] Z. Chafi, N. Keghouche, and C. Minot, *Surf. Sci.*, 601 (2007) 2323-2329.
- [32] Z. Chafi, N. Keghouche, and C. Minot, *Phys. Proc.*, 2 (2009) 673- 676.
- [33] J. E. Fallah, S. Boujana, H. Dexpert, A. Kiennemann, J. Majerus, O. Touret, F. Villain, and F.L. Normand, *J. Phys. Chem.*, 98 (1994) 5522-5533.
- [34] D. Martin and D. Duprez, *J. Phys. Chem.*, 100 (1996) 9429-9438.
- [35] D. Martin and D. Duprez, *J. Phys. Chem. B*, 101 (1997) 4428-4436.

Figure Captions

Fig.1. High resolution image of a typical ceria nanoparticle from a selected cluster of nanoparticles, (a) at 200 °C in vacuum and (b) after in-situ reduction in H₂ at 700 °C. Insets: corresponding selected area diffraction patterns and energy loss spectra from the nanoparticle cluster.

Fig.2. (a) PDC nanoparticle at 200 °C in vacuum, and (b) same nanoparticle after in-situ reduction in H₂ at 650 °C. Insets: energy loss spectra acquired from the nanoparticle.

Fig.3. A typical PDC nanoparticle at 200 °C in vacuum, and (b) another nanoparticle from the same sample after *ex-situ* reduction in 0.05 volume fraction of hydrogen in helium at 900 °C for 6 h.

Fig.4. PDC nanoparticle free of defects, (a) at 200 °C in vacuum, and (b) after reduction in H₂ at 650 °C. Insets: energy loss spectra acquired from the nanoparticle.

Fig.5. (a) High resolution image of Ni-PDC interface at 420 °C in H₂ environment; (b) and (c) energy loss spectra from region next to Ni-PDC interface (Area1) and away from the interface (Area2), respectively.

Fig. 6. (a) Mechanisms of reduction zone formation: (a) Hydrogen spillover from Ni to PDC followed by surface diffusion of H atoms across PDC, (b) hydrogen spillover from Ni to PDC followed by surface oxygen diffusion to the triple phase boundary.

Table 1. Local reduction of Ce in Ni-PDC due to H-spillover

Region	Ni particle size (nm)	Distance from Ni/PDC Interface (nm)	Oxidation state of Ce
1	15	10.0 ± 3	At interface: 2.9 ± 0.1 Away : 3.3 ± 0.1
2	20	18.0 ± 3	At interface: 3.0 ± 0.1 Away : 3.8 ± 0.1
3	10	15.0 ± 3	At interface: 3.2 ± 0.1 Away: 3.5 ± 0.1
4	9	10.0 ± 3	At interface: 3.1 ± 0.1 Away: 3.3 ± 0.1

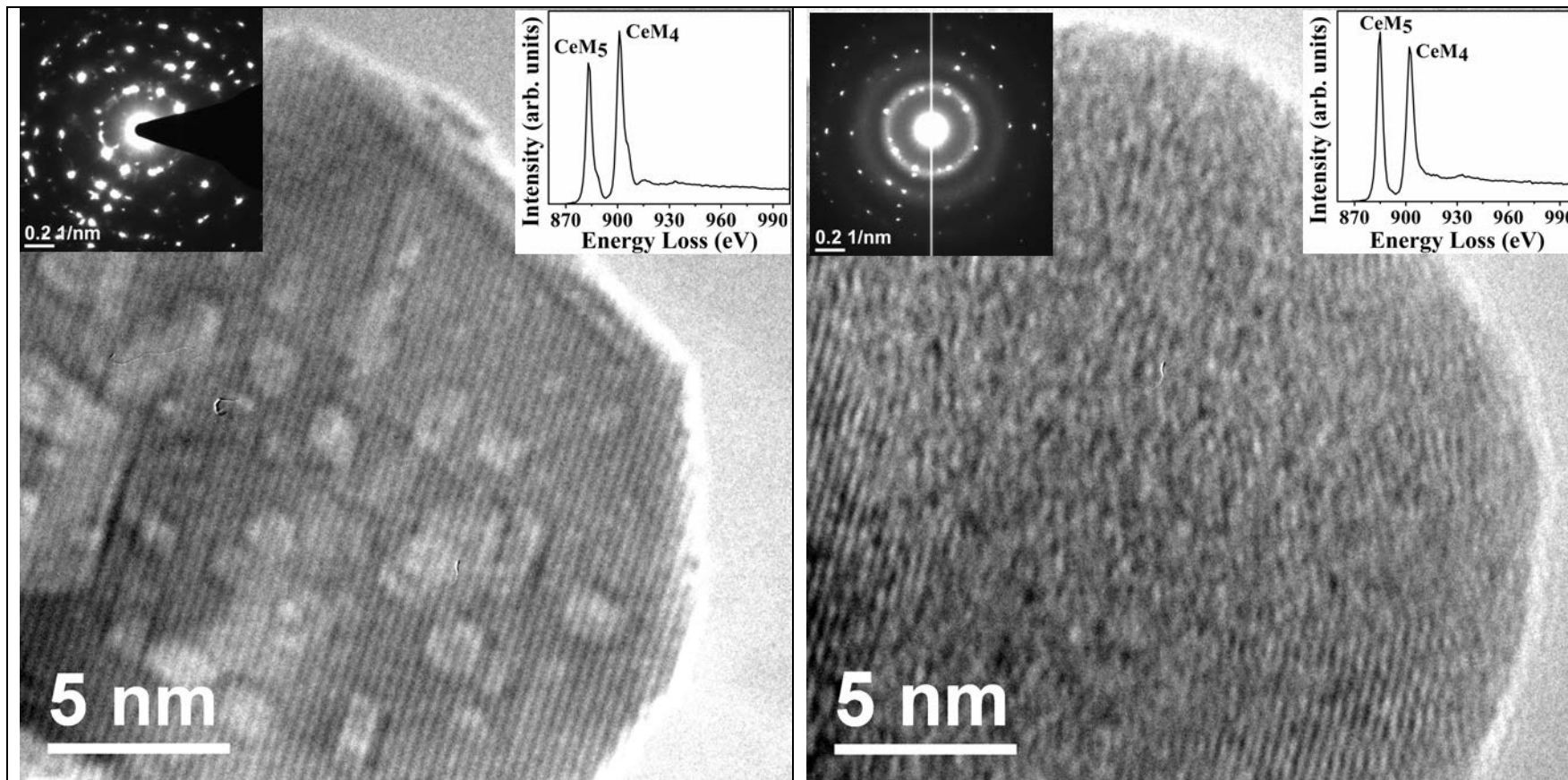


Fig.1.

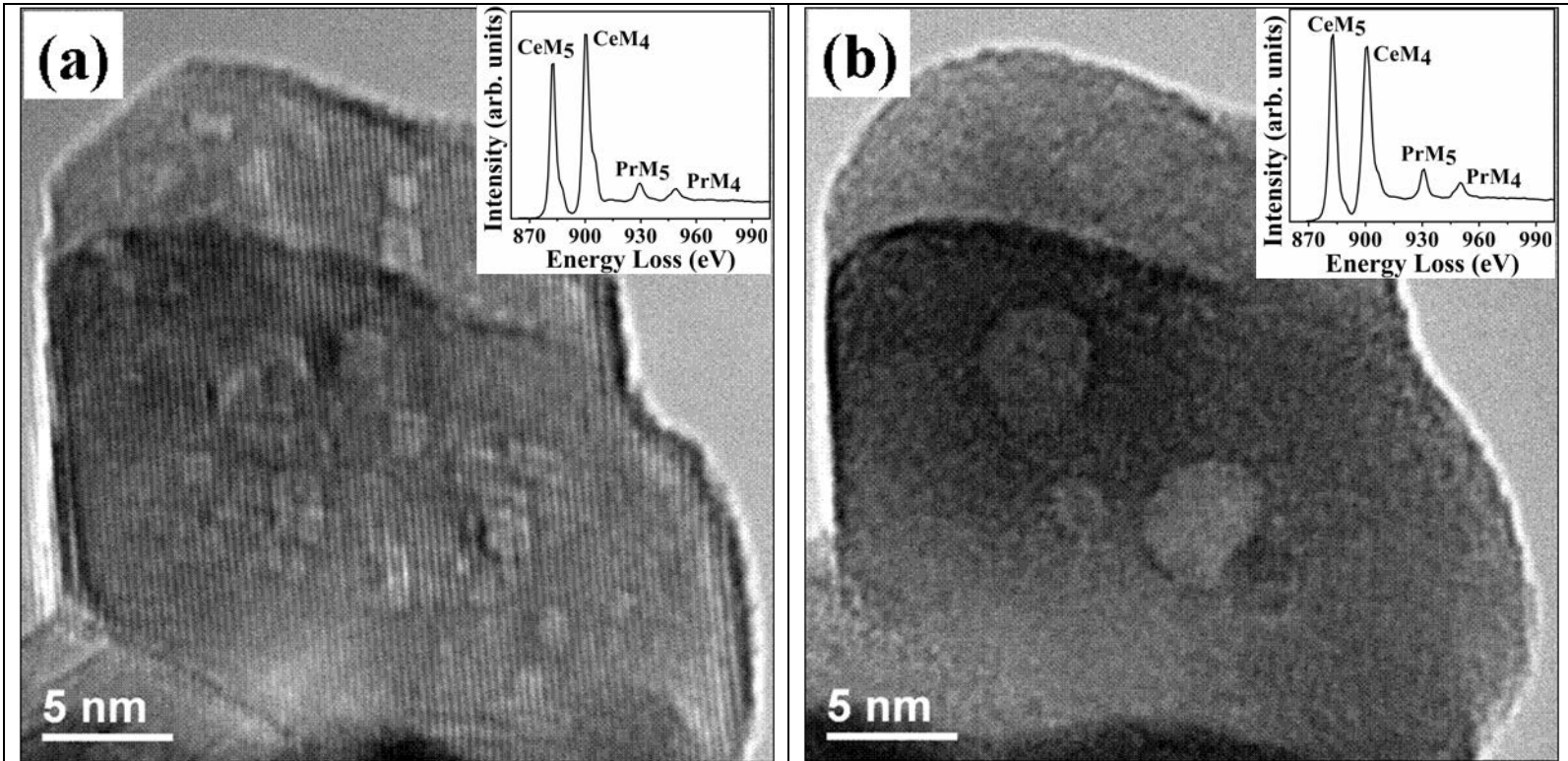


Fig.2.

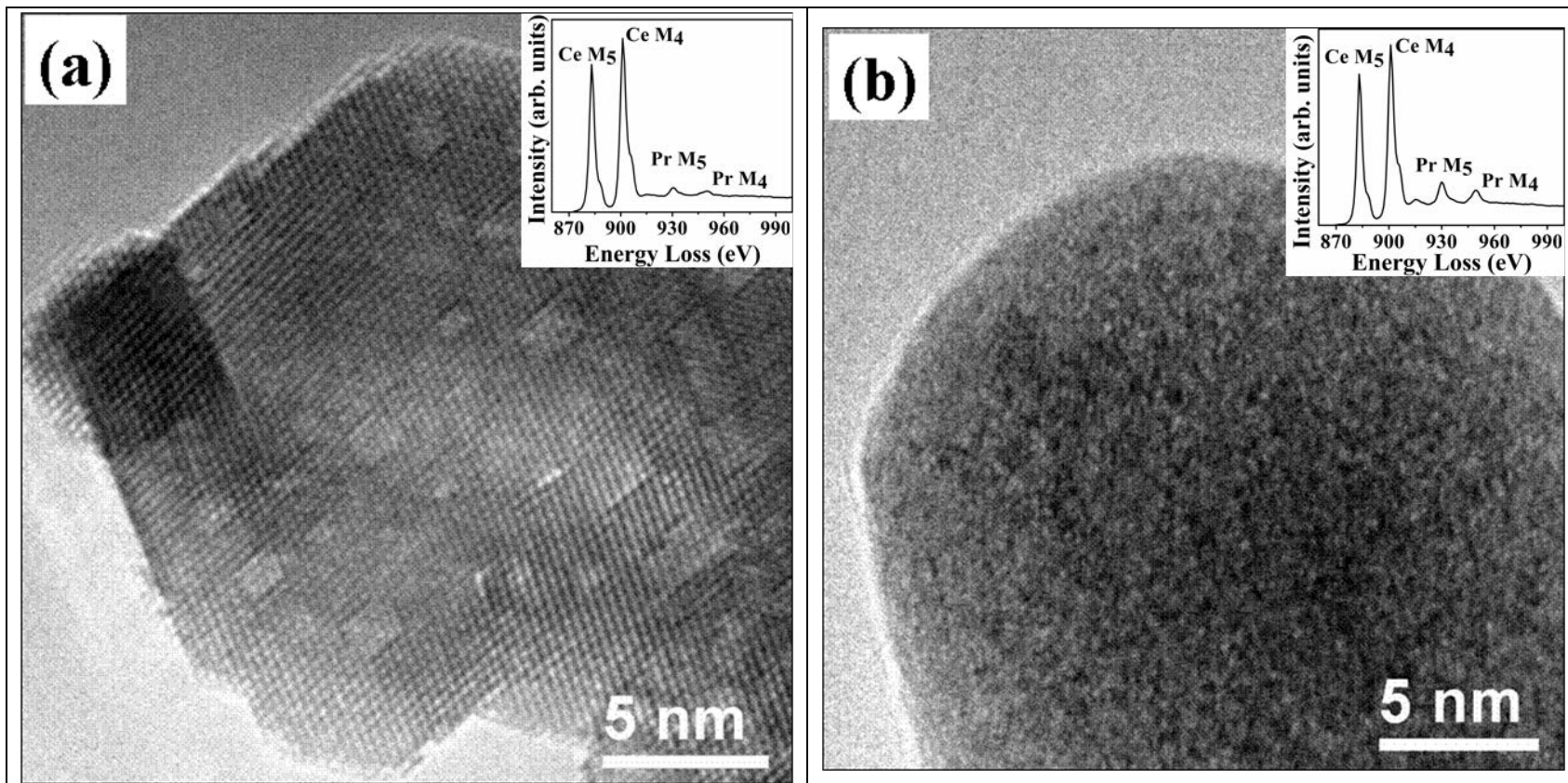


Fig.3.

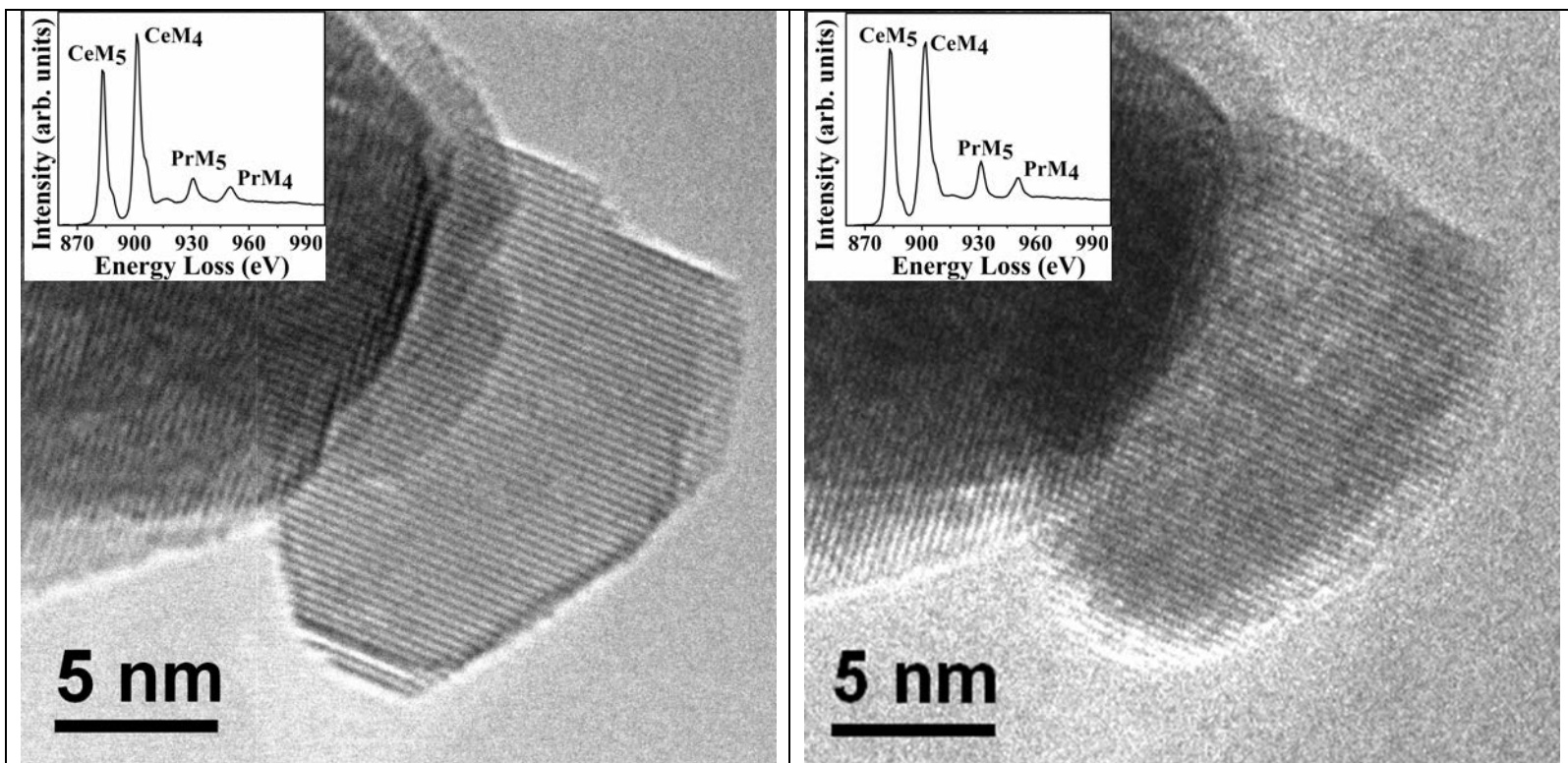


Fig.4.

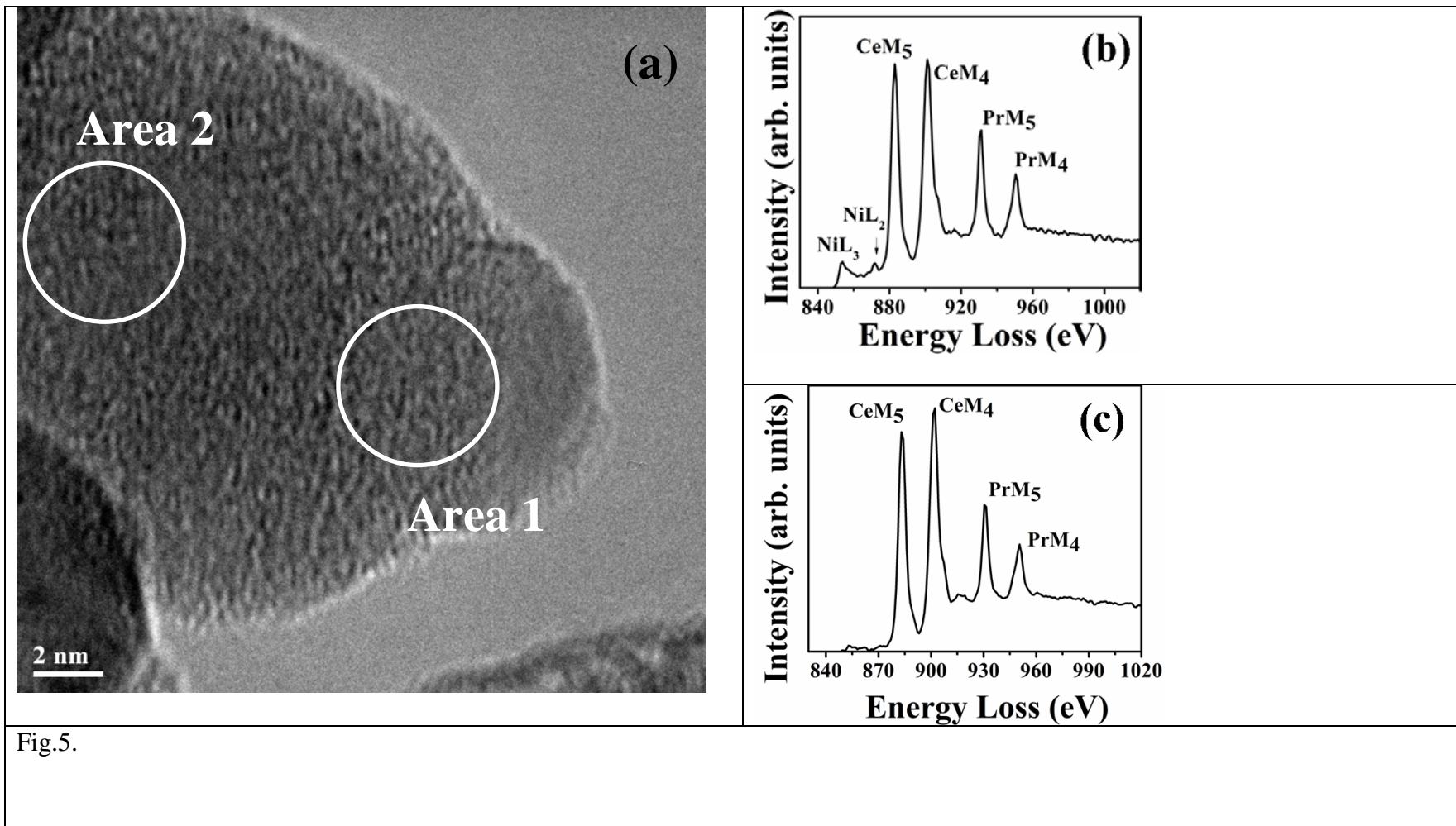


Fig.5.

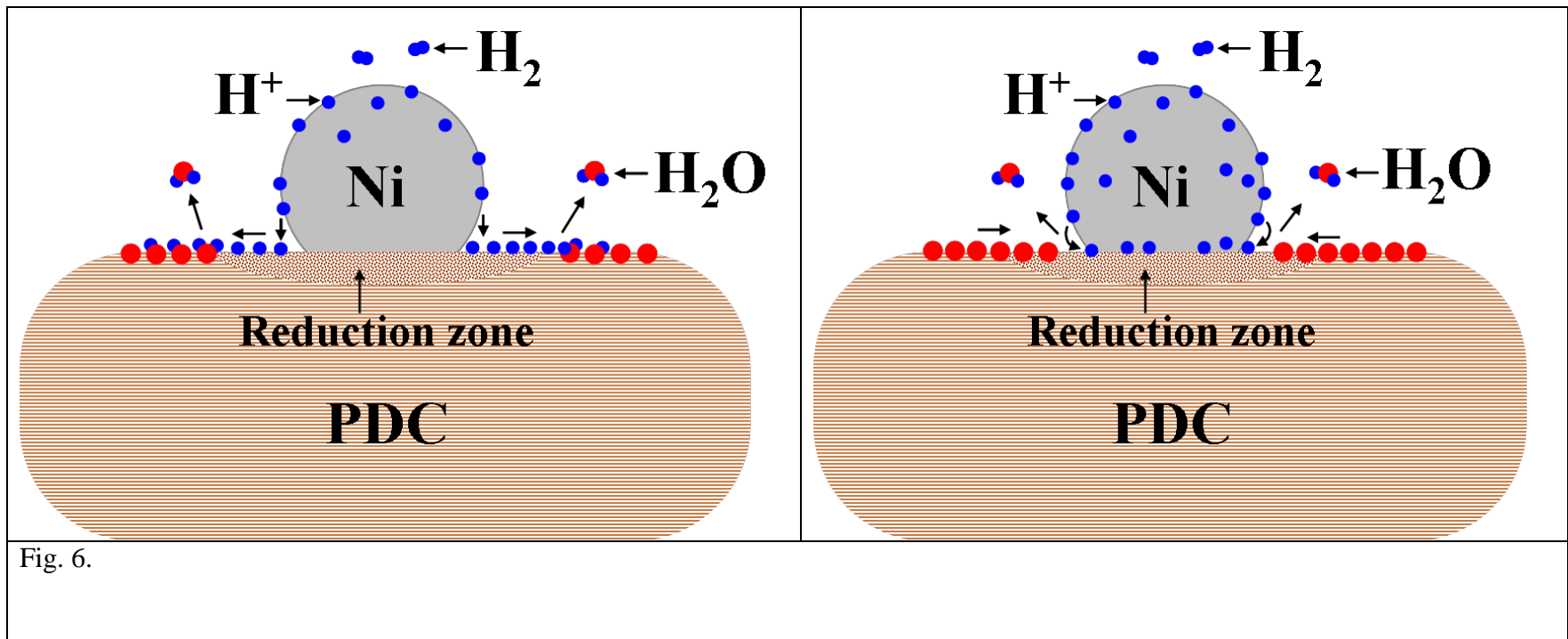


Fig. 6.